Interdisciplinary Research in Medical Sciences Specialty
ISSN: 3062-4401
2021, Volume 1, Issue 2, Page No: 26-48

Available online at: www.galaxypub.co/page/journals

Galaxy Publication

Intelligent ANFIS-PSO Prediction of Heat Transfer in Tetra-Hybrid Nanofluid Flow of Cu-CNT-Graphene-TiO_2 in Blood-Based WEG Carrier with Inclined Magnetic Field and Thermal Radiation

Anna Kowalska[1], Piotr Nowak[1], Tomasz Zieliński[1], Marek Wiśniewski[1]*

[1]Department of Biomedical Sciences, Faculty of Medicine, University of Warsaw, Warsaw, Poland.

***E-mail** ✉ marek.wisniewski.research@outlook.com

Received: 16 April 2021; **Revised:** 06 August 2021; **Accepted:** 08 August 2021

ABSTRACT

Research on heat-exchange systems for industrial and domestic use has long emphasized improving thermal transport between two parallel plates. A large body of literature stresses that boosting thermal performance is essential for both operational efficiency and cost. Increasing the Reynolds number, which intensifies turbulence, typically enhances heat conveyance. Hybrid nanofluids generally outperform single-nanoparticle fluids in thermal processes. The mixed suspension composed of Cu–CNT + Graphene + TiO_2/WEG-Blood, subjected to heat transfer between parallel plates under an inclined magnetic field and linear radiative effects, finds broad utility in engineering, biomedical, and industrial settings—including electronic thermal management, targeted drug delivery, oncology therapies, optical systems, missile and satellite components, transformer and electronic cooling, and defense-oriented solar devices. This work aims to analyze mass transport, flow behavior, and heat exchange characteristics of a Cu–CNT–Graphene–TiO_2/WEG-Blood hybrid nanofluid traveling through a porous channel influenced by linear radiation, angled magnetic forces, Forchheimer drag, and buoyancy. An ANFIS-PSO framework is adopted. Using the ODE45 solver, the governing non-dimensional, nonlinear differential equations for momentum, energy, and species concentration are integrated. The computational procedure yields temperature, velocity, and concentration fields for the hybrid Cu–CNT–Graphene–TiO_2/WEG-Blood fluid. The generated numerical patterns align well with earlier and current findings.
Thermal radiation shapes the temperature distribution within the microchannel, playing a crucial role in moderating the flow's thermal load. The radiative parameter demonstrates a suppressive effect on the temperature curve.

Keywords: ANFIS-PSO, Hybrid nanofluids, MHD, Porous, Forchheimer, Linear thermal radiation

How to Cite This Article: Kowalska A, Nowak P, Zieliński T, Wiśniewski M. Intelligent ANFIS-PSO Prediction of Heat Transfer in Tetra-Hybrid Nanofluid Flow of Cu-CNT-Graphene-TiO_2 in Blood-Based WEG Carrier with Inclined Magnetic Field and Thermal Radiation. Interdiscip Res Med Sci Spec. 2021;1(1):26-48. https://doi.org/10.51847/vjQIp7dv7B

Introduction

Nanofluids continue to attract significant scientific interest due to their enhanced thermo-physical behavior relative to standard working liquids. Their superior heating and cooling abilities have motivated extensive research on nanoparticle fabrication and fluid preparation. He *et al*. [1] evaluated ZnO–Ag thermal conductivity in a 50–50 hybrid base mixture, deriving conductivity estimates through artificial neural networks. Toghraie [2] performed experimental work on ternary nanofluids, a newer class of multi-component suspensions, using mono, biohybrid, and ternary formulations; the base mixture typically employed water and EG at an 80:20 proportion. Kristiawan *et al*. [3] investigated TiO_2/w nanofluids in helical microfin tubes and analyzed how changes in Re affected pressure reduction, reporting performance enhancements for helical microfins. Kurnia *et al*. [4] examined nanofluid behavior in straight and helical heat exchangers. Numerous reports have discussed notable thermal responses [5, 6]. Studies [7, 8] explored the roles of radiation and Lorentz forces in fluid regimes and highlighted

hybrid nanofluids' advantages for solar power systems, concluding that spectral approaches are most suitable for tackling such models.

Hybrid nanofluids, containing multiple nanoparticle types uniformly dispersed in a host liquid, typically offer better heat conduction than single-nano fluids. Consequently, they are considered more functionally advantageous. Many international research groups have recently investigated their behavior in various configurations. Indumathi *et al*. [9] examined a nanohybrid fluid over a permeable surface with suction and injection. Mburu *et al*. [10] studied nanofluid motion across porous boundaries in a 2-D incompressible stochastic turbulent setup, employing quasilinearization with bivariate spectral techniques. Shaheen *et al*. [11] analyzed hybrid-nanofluid motion between parallel plates subjected to magnetic influence and radiative heating. Ramana *et al*. [12] numerically evaluated rotating 3-D hybrid nanofluids. Dinarvand *et al*. [13] focused on mass-based hybrid nanofluid applications. Additional studies address micropolar ternary systems using Bayesian regularization [14], hybrid nanofluid transport over nonlinear stretching bases [15], Darcy-Forchheimer modifications [16], and CNT–Ferrousoxide/water mixtures under variable magnetic intensity [17].

When analysing transport phenomena in porous structures, Darcy's law is commonly applied as the foundational framework. Forchheimer later introduced an additional nonlinear correction to account for reduced apparent permeability, as noted in Ref. [18], resulting in what is now referred to as the Darcy–Forchheimer formulation, which incorporates inertial contributions. Muskat and Wyckoff [19] established uniform flow characteristics for fluids passing through Darcy-type materials. Seddeek [20] explored the combined influences of thermophoresis and viscous dissipation on convection in Darcy flows, concluding that an increase in thermophoretic parameters enlarges the boundary layer while simultaneously diminishing fluid velocity. Sadiq and Hayat [21] examined magnetically influenced two-dimensional motion of Maxwell fluids over a surface undergoing linear stretching, revealing that both the Prandtl number and thermal relaxation factors inversely affect temperature distribution.

Hayat *et al*. [22] investigated nanofluid movement in a porous medium following Darcy behaviour with chemical reactivity. Rasool *et al*. [23] studied nanofluid transport between two horizontal plates embedded in a Darcy–Forchheimer environment under a uniform magnetic field. Their results indicate that enhanced viscosity parameters reduce temperature fields, whereas Brownian motion and thermophoresis intensify. Moreover, greater porosity values lead to higher surface drag forces.

Biochemical reactions in living organisms are facilitated by numerous enzymes and have significant implications for medical science. Blood flow modelling often depends on both in vivo and in vitro assessments of chemical interaction effects. Tripathi and Sharma [24] focused on the pulsatile motion of blood through a stenosed artery. Recently, several computational techniques have been deployed for simulating complex hydrodynamic systems and processing tasks, such as response surface methodology, support vector machines, artificial neural networks, and adaptive neuro-fuzzy inference systems (ANFIS) as reported in Ref. [25]. Long *et al*. [26] optimized neural-network-based frameworks to evaluate the stability of Al_2O_3–ethylene glycol nanofluids. Earlier studies demonstrate that ANFIS generally surpasses RSM when limited datasets are available for modelling experimental behaviour [27–29].

Li, Z.X. [30] compared ANFIS, neural networks, regression tools, and experimental outputs for nanofluids used as secondary fluids in refrigeration. Selimefendigil *et al*. [31] implemented numerical simulations and ANFIS modelling for mixed convection of CNT–water nanofluid in a branched duct containing an annulus and a rotating inner boundary. Xianqin Li *et al*. [32] assessed thermal augmentation using a hybrid nanofluid composed of titanium oxide and aluminium oxide nanoparticles; these hybrid particles were synthesized by blending kerosene oil with water-derived constituents. Shuhe Sun *et al*. [33] and Mahantesh *et al*. [34] discussed the importance of viscous and Joule heating on MoS_2–Ag hybrid nanofluid flow over an isothermal wedge.

Novelty of the current study

Within biomedical applications, interactions among Cu–CNT–Graphene–TiO_2/WEG-Blood nanoparticles have not yet been documented. Hybrid nanofluid models using two-component nanoparticles inside porous channels remain unexplored, presenting a significant scientific gap. This study addresses that gap by incorporating ANFIS-PSO, inclined magnetic fields, permeable Reynolds effects, porous-medium behaviour, Forchheimer resistance, linear radiation, and buoyancy to evaluate biobased nanofluid dynamics. Similarity transformations were used to refine the hybrid nanofluid characteristics, and the governing system was solved through the ODE45 numerical scheme. A comprehensive assessment of how various physical parameters influence the model's dynamic response is provided. The model's ANFIS predictive capability is further strengthened by integration with PSO.

Mathematical formulation

The governing expressions developed here follow the methodologies presented by Vijayalakshmi and Srinivas [35] and Hamidreza Shojaie *et al*. [36].

$$\frac{\overline{\partial v}}{\partial y}+\frac{\overline{\partial u}}{\partial x}=0 \tag{1}$$

$$\overline{u\frac{\partial \bar{u}}{\partial x}}+\bar{v}\frac{\overline{\partial u}}{\partial y}+\frac{\overline{\partial u}}{\partial t}=-\frac{1}{P_{Thnf}}\frac{\partial_{p}}{\partial_{x}}-\frac{\mu_{Thnf}{}^{\Phi}}{P_{Thnf}{}^{k}}\bar{u}-\frac{\sigma B_{0}{}^{2}\bar{u}}{P_{Thnf}}\cos^{2}\Omega+\frac{\mu_{Thnf}}{P_{Thnf}}\left(\frac{\partial^{2}\bar{u}}{\partial x^{2}}+\frac{\partial^{2}\bar{u}}{\partial y^{2}}\right)-\frac{Cb}{x\sqrt{k}}\bar{u}^{2}+g(\rho\beta)Thnf(T-T_{u})\bar{u} \tag{2}$$

$$\overline{\bar{u}\frac{\partial T}{\partial x}}+\bar{v}\frac{\partial T}{\partial y}+\frac{\partial T}{\partial t}=-\frac{1}{P_{Thnf}}\left(\frac{\partial q}{\partial y}\right)-\left(\frac{\mu_{Thnf}}{\rho_{Thnf}}\right)\left(\frac{\Phi}{k}\right)\bar{v}-\frac{\sigma B_{0}2^{\bar{\bar{V}}}}{P_{Thnf}}\cos^{2}\Omega+\left(\frac{\partial^{2}\bar{V}}{\partial x^{2}}+\frac{\partial^{2}\bar{V}}{\partial y^{2}}\right)\left(\frac{\mu_{Thnf}}{P_{Thnf}}\right)-\frac{Cb}{x\sqrt{k}}\overline{V^{2}} \tag{3}$$

$$\bar{u}\frac{\partial T}{\partial x}+\bar{v}\frac{\partial T}{\partial y}+\frac{\partial T}{\partial t}=\frac{k_{Thnf}}{(\rho C_{p})_{Thnf}}\left(\frac{\partial^{2}T}{\partial y^{2}}\right)+\frac{Q_{0}(T-T_{u})}{(\rho C_{p})_{Thnf}}-\left[\frac{1}{(\rho C_{p})_{Thnf}}\frac{\partial q_{r}}{\partial y}\right] \tag{4}$$

The following boundary constraints are adopted in accordance with the formulation provided by Kumar *et al*. [37].

$$at\ \bar{v}=-\overline{v_{l}}=-A_{0}\dot{h},y=-h(t),T=T_{u}and\bar{u}=0, \tag{5}$$

$$at\ \bar{v}=-\overline{v_{u}}=-A_{1}\dot{h},y=h(t),T=T_{l}and\bar{u}=0, \tag{6}$$

Where $A_{1}=\frac{\overline{v_{u}}}{h}$ the permeability of the wall.

Where,

$$D_{2}=\frac{\rho_{Thnf}}{\rho_{f}},D_{1}=\frac{\mu_{Thnf}}{\mu_{f}},D_{3}=\frac{k_{Thnf}}{k_{f}},D_{4}=\frac{(\rho C_{p})_{Thnf}}{(\rho C_{p})_{f}},D_{3}=\frac{(\rho\beta)_{Thnf}}{(\rho\beta_{p})_{f}}$$

Mean flow rate functions and stream functions.

$$\bar{v}=-\psi_{x},\bar{u}=\psi_{y} \tag{7}$$

$$\psi=\nu xf(\xi,t)h,\bar{u}=\nu xh2f\xi(\xi,t),\bar{v}=-\nu hf(\xi,t). \tag{8}$$

Where $f_{\xi}=\left(\frac{\partial f}{\partial \xi}\right),\xi=\left(\frac{y}{h}\right)$,

The Roselands approximation for radiation can be used to simplify radiative heat transfer.

$$q_{r}=-\left(\frac{4\sigma}{3k}\right)\left(\frac{\partial T^{4}}{\partial y}\right) \tag{9}$$

Here σ is Stefan-constant. Boltzmann's k, the typical absorption rate, B is the constant of the fluid, and m_1 is the power law index of the temperature.

$$T^{4}\cong -3T_{l}^{4}+4TT_{l}^{3},T=T_{l}+B\left(\frac{x}{h}\right)^{m_{1}}\theta(\xi) \tag{10}$$

The following is the temperature that has no dimensions.

$$\frac{T-T_{l}}{T_{U}-T_{l}}=\theta \tag{11}$$

The set of dimensionless governing equations has the following structure:

$$\frac{d^4f}{d\xi^4}+\alpha\left(\frac{D_1}{D_2}\right)\left[\xi\frac{d^3f}{d\xi^3}+3\frac{d^2f}{d\xi^2}\right]-M^2f'(\xi)\cos^2\Omega+\left(\frac{D_1}{D_2}\right)\mathrm{Ref}(\xi)\frac{d^3f}{d\xi^3}-\left(\frac{D_1}{D_2}\right)\mathrm{Re}\frac{df}{d\xi}\frac{d^2f}{d\xi^2}-\frac{1}{\varepsilon}\frac{d^2f}{d\xi^2}-\mathrm{Fr}\frac{d^2f}{d\xi^2}+D_5\beta f\,\theta=0 \quad (12)$$

$$\left[\frac{D_3}{D_4}+\frac{4}{3}\frac{Rd}{D_4}\right]\frac{1}{Pr}\frac{d^2\theta}{d\xi^2}+\alpha\left(\xi\frac{d\theta}{d\xi}+m_1\theta\right)-m_1\mathrm{Re}\frac{df}{d\xi}\theta(\xi)+\mathrm{Re}\,f(\xi)\frac{d\theta}{d\xi}=0 \quad (13)$$

The following are the relevant boundary conditions [37]:

$$\theta(-1)=1, f(-1)=A, f'^{(-1)}=0 \text{and } \theta(1)=0, f'(1)=0. \quad (14)$$

The study's dimensionless parameters are

$\mathrm{Pr}=\frac{\mu_{f(Cp)}}{k_f}$ Prandtl number, $M=\frac{\sigma B_0^2}{\rho_f h}$ Magnetic parameter, $\mathrm{Rd}=\frac{4\sigma T_0^3}{kk_f}$ ThermalRadiation,

$\varepsilon=\frac{k}{\Phi h^2}$ 2 Darcian paraneter, $\alpha=\frac{hh}{v_f}$ Walleaxpansionratio, $\mathrm{Re}=\frac{Ahh^{\cdot}}{v_f}$ hhνfPermeableReynoldsnumber, $Q=\frac{Q_0}{(\rho cp)_{fh}}$ $\frac{\text{Heatsource}}{\text{sink}}$, $\mathrm{Fr}=\frac{Cb}{\sqrt{k}}$ Forchheimernumber, $\beta=\frac{g\beta(T_1-T_u)}{\overline{hu}}$ Grashofnumber.

The following are the definitions of Nusselt number and dimensionless Skin friction [37].

$$\mathrm{Nu}=-\left[D3+\frac{4}{3}\mathrm{Rd}\right]\theta'(\xi)_{\xi=-1,1}\ , Cf_x=\frac{D_1}{D_2}f''(\xi)_{\xi=-1,1} \quad (15)$$

Once the flow field has been identified, the momentum equation (3) can be modified to get the normal pressure gradient by adding the velocity component.

$$\frac{\partial_p}{\partial_y}=-\frac{\rho_{Thnf}}{\rho_f}\left[\alpha(f+yf_y)\mathrm{Re}^{-1}+ff_y+\frac{\mu_{Thnf}}{\rho Thnf}\frac{1}{vf}\mathrm{Re}^{-1}ff_y-\frac{-\sigma B0}{\rho Thnf}-\frac{Cb}{\sqrt[x]{k}}V^{-2}\right], p=\frac{\bar{p}}{\rho_f v_w^2}. \quad (16)$$

It is now possible to find the normal pressure distribution by integrating equation (16), letting pc be the centre line pressure. Acknowledging that $ff_y=\frac{1}{2}(f^2)'$ and $(f+yf_y)=(yf)'$, hence [36]:

$$\int_{pc}^{p(y)}dp=\int_0^y-\frac{\rho_{Thnf}}{\rho_f}\left[\frac{\alpha}{\mathrm{Re}}(yf)'+\left(\frac{f^2}{2}\right)'+\frac{\mu_{Thnf}}{\rho Thnf}\frac{1}{vf}\mathrm{Re}^{-1}f-\frac{-\sigma B0}{\rho Thnf}-\frac{Cb}{\sqrt[x]{k}}V^{-2}\right]dy \quad (17)$$

Normal pressure will be as follows [36]:

$$\Delta_{pn}=-\frac{\rho Thnf}{\rho f}\left[\frac{\alpha}{\mathrm{Re}}(yf)+\left(\frac{f^2}{2}-\frac{f^2(0)}{2}\right)\right]-\frac{\mu_{Thnf}}{\mu_f}\left(\frac{1}{\mathrm{Re}}(f'-f'(0))\right)-\frac{1}{\rho_f}M^2[f-f(0)]\cos^2\Omega-D_2\mathrm{Fr}[f''-f''(0)]. \quad (18)$$

Reliability of the numerical solution and dimensionless equations

The MATLAB in-built solver ODE45 was employed. The transformed Equations 12 and 13 were computed under the boundary conditions given in (14) using ODE45. To perform this procedure, the following assumptions are considered:

$$f=h_1., \theta=h_5, \chi=h_6, \chi'=h_7, f'=h_2, \theta'=h_6, f''=h_3, f'''=h_4.$$

Implementation of boundary conditions

$f_a(1)=A, f_a(6), f_a(2)=0, f_a(5)=1$

$f_b(1)=1, f_b(6), f_b(2)=0, f_b(5)=0.$

Results and Discussion

Effect of dimensionless parameters on velocity, temperature, and concentration profiles

This part explores how different dimensionless quantities influence the distributions of velocity, temperature, and concentration in two distinct cases. Case 1 consists of CNT + Graphene + Cu + TiO_2 nanoparticles dispersed in WEG, while Case 2 uses the same nanoparticles in Blood as the base fluid. The bvp4c method was applied to compute the profiles under the following ranges of parameters: $0.4 \le \beta \le 1.9$; $0.3 \le \varepsilon \le 1.2$; $0.9 \le Fr \le 3.6$; $0.2 \le M \le 1.1$; $0.1 \le Q \le 0.7$; $0.6 \le Rd \le 2.4$; $1.0 \le Re \le 4.0$.

Summary of Tables and Figures:

- **Table 1**: Lists the thermophysical characteristics of the nanoparticles and base fluids.
- **Table 2**: Provides the correlations for dynamic viscosity, density, specific heat, and thermal expansion.
- **Table 3**: Shows important component parameters at various threshold values.
- **Table 4**: Details the design and outcomes of the heat transfer experiment (Nusselt number).
- **Figure 1**: Illustrates the geometric and physical model.
- **Figures 2 and 3**: Present the dimensionless velocity f '(ξ) and temperature θ(ξ) for different β values in both groups.

Analysis of **Figure 2** shows that increasing β leads to higher f '(ξ) near the center of the momentum boundary, with the flow profile exhibiting symmetry about the midpoint. **Figure 3** demonstrates that θ(ξ) grows markedly with increasing β in both cases. Notably, Group II (Blood as the base fluid) exhibits thicker permeable boundary layers, producing higher temperature magnitudes. In axisymmetric flows, as the Grashof number rises, buoyancy effects become more influential, resulting in a mixed velocity field governed by both natural and forced convection. The thickening of the thermal boundary layer is primarily driven by stronger convective heat transfer, which aligns with the temperature variations reported in **Table 2**.

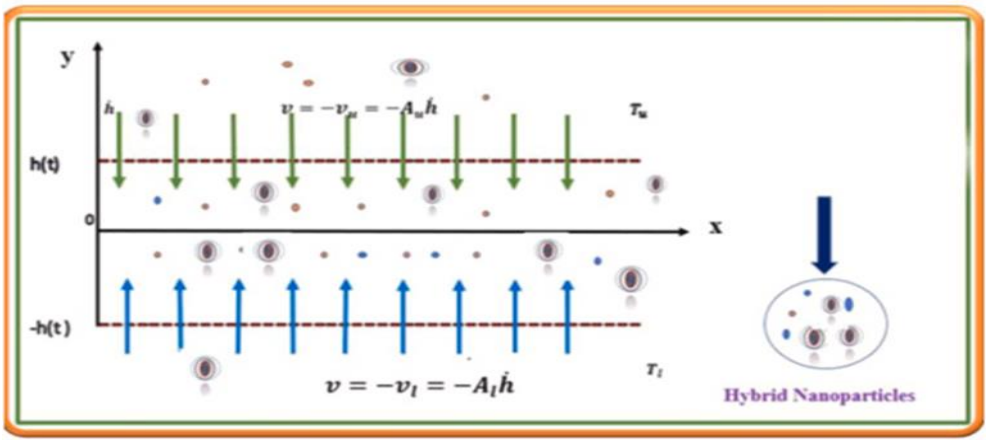

Figure 1. Physical abstract.

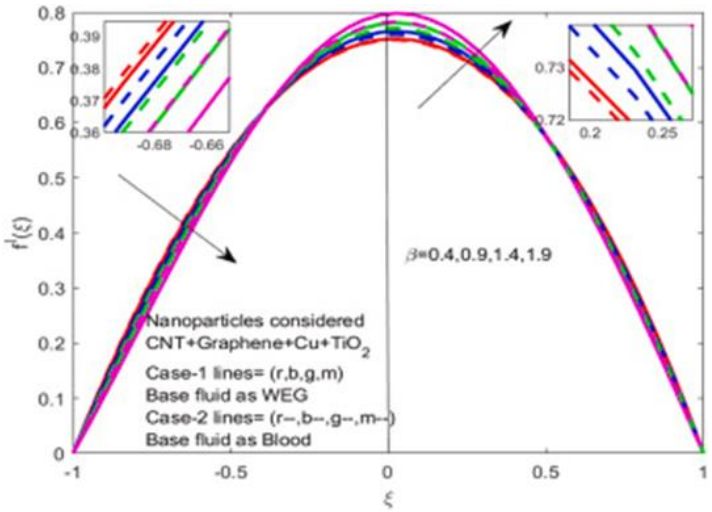

Figure 2. $f'(\xi)$ with the impact of β

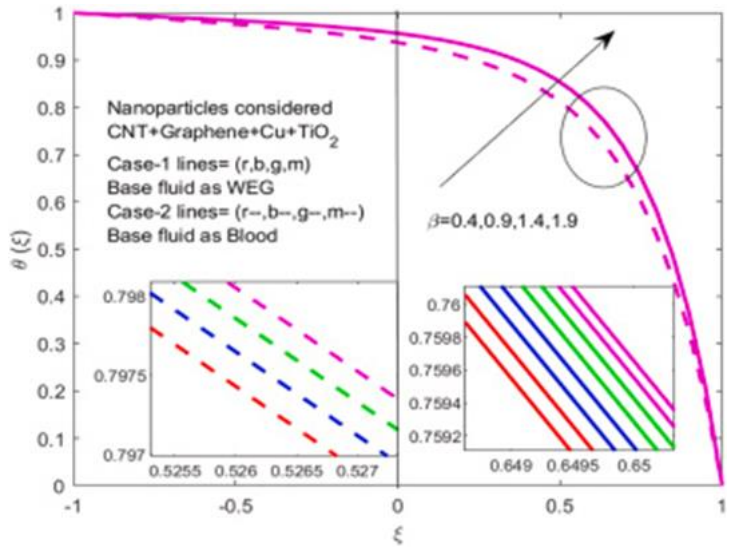

Figure 3. (ξ) with the impact of β

Table 1. Thermophysical characteristics of hybrid nanofluids.

Thermophysical Properties of Base Fluids and Tetra-Hybrid Nanoparticles	Thermal Conductivity (k, W/m·K)	Density (ρ, kg/m³)	Specific Heat Capacity (Cp, J/kg·K)
Base Fluids			
Water-Ethylene Glycol (WEG)	0.18166	1041.89	3421.54
Human Blood	0.492	1064	3594
Tetra-Hybrid Nanoparticles			
Titanium Dioxide (TiO_2)	8.953	4250	690
Graphene	5000	2200	790
Carbon Nanotubes (CNT)	3007.4	5100	410
Copper (Cu)	400	8933	385

Case 1: CNT + Graphene + Cu + TiO_2 nanoparticles in WEG as the base fluid.
Case 2: CNT + Graphene + Cu + TiO_2 nanoparticles in Blood as the base fluid.

Table 2. Relations for dynamic viscosity, density, specific heat, and thermal expansion.

S.No	Model name	Relations
1	Dynamic viscosity	$\mu_{Thnf} = \mu_f\{(1-\varphi_1)2.5(1-\varphi_2)2.5(1-\varphi_3)2.5(1-\varphi_4)^{2.5}\}^{-1}$
2	Density	$\rho_{Thnf} = \{(1-\varphi_4)((1-\varphi_3)((1-\varphi_2)((1-\varphi_1)+\frac{\varphi_1\rho_{s1}}{\rho_f})+\frac{\varphi_2\rho_{s2}}{\rho_f})+\frac{\varphi_3\rho_{s3}}{\rho_f})+\frac{\varphi_4\rho_{s4}}{\rho_f}\}$
3	Heat Capacity	$(\rho C_p)_{Thnf} = \left\{(1-\varphi_4)\left\{\frac{\varphi_3(\rho C_p)_{s3}}{(\rho C_p)_f}\left((1-\varphi_3)\left((1-\varphi_2)+\frac{\varphi_1(\rho C_p)_{s1}}{(\rho C_p)_f}+\cdots\right)+\frac{\varphi_4(\rho C_p)_{s4}}{(\rho C_p)_f}\right)+\frac{\varphi_4(\rho C_p)_{s4}}{(\rho C_p)_f}+\cdots.\right)+\cdots\right\}$

4	Thermal expansion	$((\rho\beta)_{\text{Thnf}} = \left\{ (1-\varphi_4)\left\{ \frac{\varphi_3(\rho C_p)_{s3}}{(\rho C_p)_f}\left(\frac{(1-\varphi_3)}{(1-\varphi_2)((1-\varphi_3)+\frac{\varphi_1(\rho C_p)_{s1}}{(\rho C_p)_f}+\cdots} \right) + \cdots . \right) + \cdots \right\}$
5	Thermal Conductivity	$\frac{k_{Thnf}}{k_f} = \frac{(k_{s4}+2k_{ternary}-2\varphi_4(k_{ternary}-k_{s4}))}{(k_{s4}+2k_{ternary}+\varphi_4(k_{ternary}-k_{s4}))}$; $\frac{k_{Thnf}}{k_f} = \frac{(k_{s3}+2k_{hybrid}-2\varphi_3(k_{hybrid}-k_{s3}))}{(k_{s3}+2k_{hybrid}+\varphi_3(k_{hybrid}-k_{s3}))}$; $\frac{k_{Thnf}}{k_f} = \frac{(k_{s2}+2k_{nano}-2\varphi_2(k_{nano}-k_{s2}))}{(k_{s2}+2k_{nano}+\varphi_2(k_{nano}-k_{s2}))}$; $\frac{k_{Thnf}}{k_f} = \frac{(k_{s1}+2k_f-2\varphi_1(k_f-k_{s1}))}{(k_{s1}+2k_f+\varphi_1(k_f-k_{s1}))}$.

Table 3. Essential component characteristics with varying threshold values.

Key Factors	Low Level	Medium Level	High Level	Symbol
Thermal radiation parameter	0.6	1.2	1.8	Rd (Z_1)
Heat source/sink parameter	0.1	0.3	0.5	Q (Z_2)
Reynolds number	1	2	3	Re (Z_3)

Table 4. Experimental design and results for heat transfer rates (Nusselt number).

Run	Coded Z1	Coded Z2	Coded Z3	Rd	Q	Re	Nusselt Number (Case-1, Predicted)	Nusselt Number (Case-2, Predicted)	Nusselt Number (Case-1, True)	Nusselt Number (Case-2, True)
1	−1	−1	−1	0.6	1	0.1	1.414356	1.440721	1.507112	1.628931
2	1	−1	−1	1.8	1	0.1	1.111729	1.227229	1.139477	1.189272
3	−1	1	−1	0.6	3	0.1	1.092592	1.021446	1.031011	1.046022
4	1	1	−1	1.8	3	0.1	1.089349	1.006061	1.006253	1.010052
5	−1	−1	1	0.6	1	0.3	1.712397	1.164946	1.954011	1.133793
6	1	−1	1	1.8	1	0.3	1.139737	1.158393	1.123993	1.327019
7	−1	1	1	0.6	3	0.3	1.332809	1.405041	1.312926	1.541221
8	1	1	1	1.8	3	0.3	1.483185	1.701583	1.520426	1.776125
9	−1	0	0	0.6	2	0.2	1.712543	1.479101	1.408570	1.570875
10	1	0	0	1.8	2	0.2	1.666667	1.592591	1.411787	1.574549
11	0	−1	0	1.2	1	0.2	1.600462	1.451282	1.414894	1.578106
12	0	1	0	1.2	3	0.2	1.299213	1.208289	1.217962	1.551612
13	0	0	−1	1.2	2	0.1	1.434831	1.522082	1.610561	1.287613
14	0	0	1	1.2	2	0.3	1.416666	1.521221	1.436942	1.581612
15	0	0	0	1.2	2	0.2	1.330245	1.925925	1.417962	1.917343
16	0	0	0	1.2	2	0.2	1.330245	1.925925	1.417962	1.917343
17	0	0	0	1.2	2	0.2	1.330245	1.925925	1.417962	1.917343
18	0	0	0	1.2	2	0.2	1.330245	1.925925	1.417962	1.917343
19	0	0	0	1.2	2	0.2	1.330245	1.925925	1.417962	1.917343
20	0	0	0	1.2	2	0.2	1.330245	1.925925	1.417962	1.917343

Figures 4 and 5 illustrate the dimensionless velocity f '(ξ) and temperature θ(ξ) for different values of the

parameter ε in both groups: Group I (CNT + Graphene + Cu + TiO_2 in WEG) and Group II (CNT + Graphene + Cu + TiO_2 in Blood). From **Figure 4**, increasing ε leads to higher f '(ξ) in the center of the momentum boundary, with the flow pattern maintaining symmetry. **Figure 5** shows that θ(ξ) rises substantially with increasing ε for both groups, with Group II exhibiting thicker permeable boundary layers from the lower to the upper plate, resulting in elevated temperatures.

As the Darcy parameter increases in axisymmetric flow, heat retention is enhanced, raising the temperature profile. Meanwhile, the concentration profile decreases because higher flow rates dilute the reactant concentration. The velocity profile shows mixed behavior due to variable resistance in the porous medium.

Figures 6 and 7 present the influence of the Forchheimer parameter (Fr) on f '(ξ) and θ(ξ), considering $0.9 \leq Fr \leq 3.6$. **Figure 6** shows that higher Fr reduces f '(ξ) near the lower surface while increasing it near the upper surface. In **Figure 7**, the temperature distribution declines at both boundaries as Fr increases. This occurs because stronger Forchheimer resistance reduces heat transfer and alters reactant distribution within the axisymmetric porous medium.

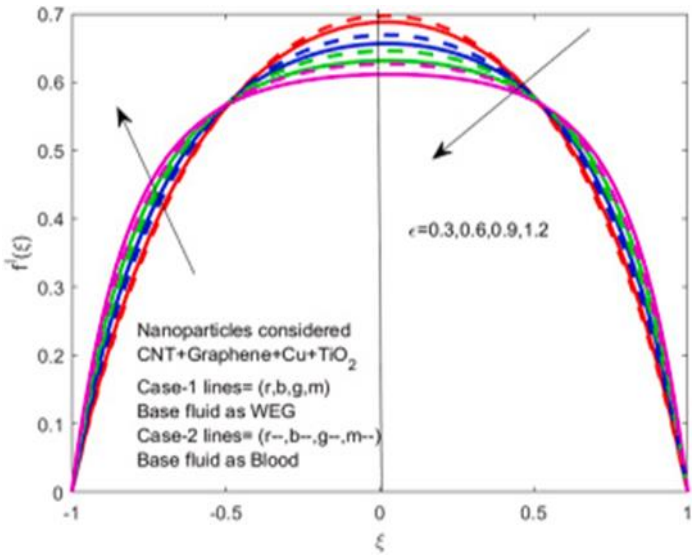

Figure 4. $f'(\xi)$ with the impact of ε

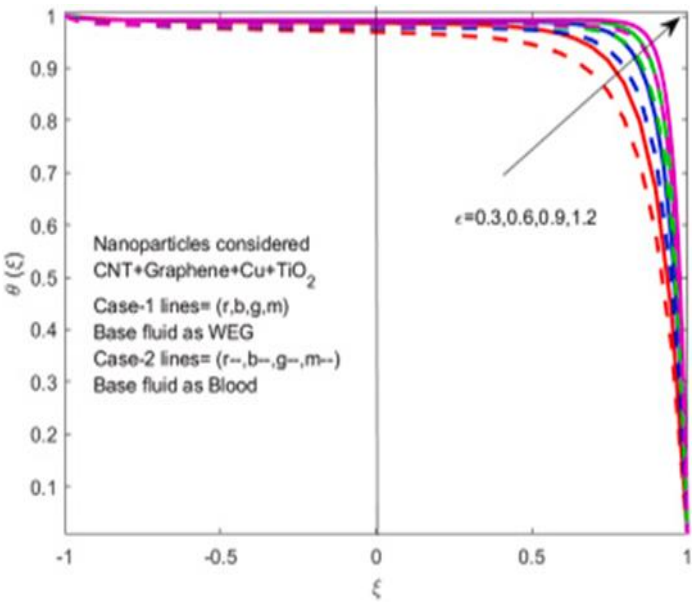

Figure 5. (ξ) with the impact of ε

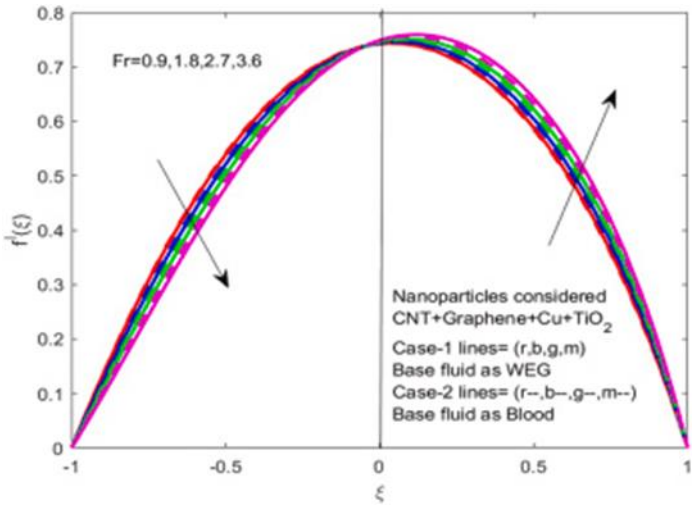

Figure 6. $f'(\xi)$ with the impact of Fr

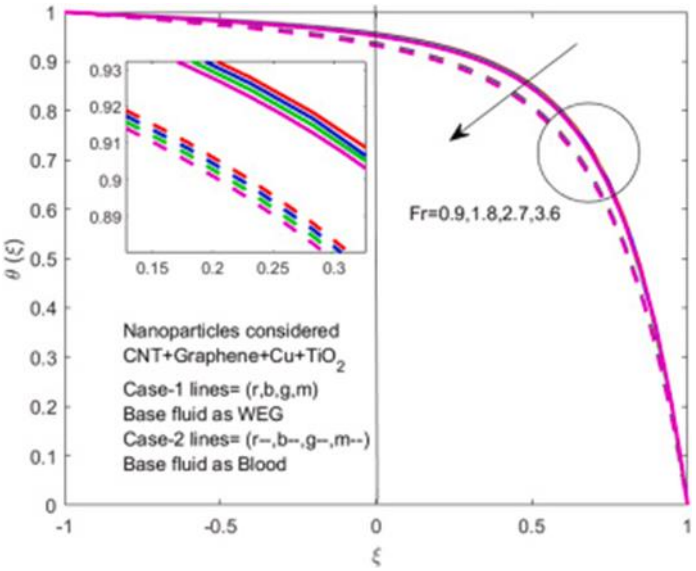

Figure 7. (ξ) with the impact of Fr

In contrast, the velocity distribution exhibits a mixed pattern due to nonlinear drag effects. **Figures 8 and 9** show the influence of the magnetic parameter M on f '(ξ) and θ(ξ) for $0.2 \leq M \leq 1.1$. **Figure 8** indicates that increasing M enhances f '(ξ) near the middle of the channel but decreases it near the lower boundary and diminishes slightly at the upper boundary. Physically, a stronger magnetic field generates larger Lorentz forces, which resist fluid motion and reduce momentum. **Figure 9** illustrates θ(ξ), where temperature rises at both lower and upper surfaces as M increases, reflecting the heating effect of the magnetic field. Overall, the axisymmetric velocity profile demonstrates mixed behaviour due to the Lorentz-induced modification of the fluid motion.

Figure 10 depicts θ(ξ) under varying Q. As Q grows, θ(ξ) increases, with the temperature effect being more pronounced in CNT + Graphene + Cu + TiO_2 with WEG compared to Blood. In an axisymmetric flow, higher heat source/sink values elevate the temperature because a heat sink slows cooling or a heat source adds energy, thereby raising the system's thermal level.

Figures 11 and 12 examine the role of the radiation parameter Rd on f '(ξ) and θ(ξ). In **Figure 11**, increasing Rd boosts fluid velocity near the lower boundary while reducing it at the upper boundary. For Blood-based nanofluids, the upper region of the channel displays higher velocity than the lower region, whereas WEG-based nanofluids show the opposite trend. **Figure 12** shows that higher Rd values decrease θ(ξ), as the combined effects of radiative heat loss and fluid motion lead to reduced energy within the system. Consequently, the axisymmetric velocity shows mixed behaviour, while the temperature declines with stronger radiation.

Figures 13 and 14 present the effect of the permeable Reynolds number (Re) on f '(ξ) and θ(ξ) for both groups.

As Re increases, θ(ξ) rises throughout the channel, with WEG-based nanofluids showing higher temperatures than Blood-based ones. The velocity profile maintains a mixed character due to the interplay of inertial and viscous forces in the porous medium. In axisymmetric flow, enhanced Re improves convective transport, which elevates the temperature distribution, while the velocity pattern remains complex because of porous resistance **(Figure 17)**.

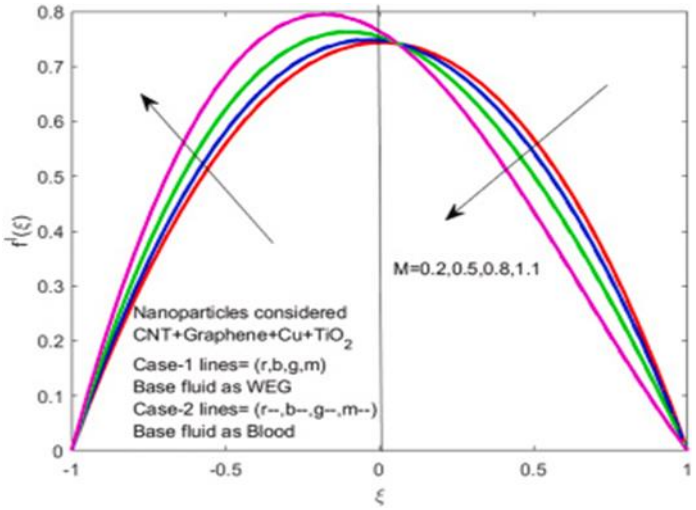

Figure 8. $f'(\xi)$ with the impact of M

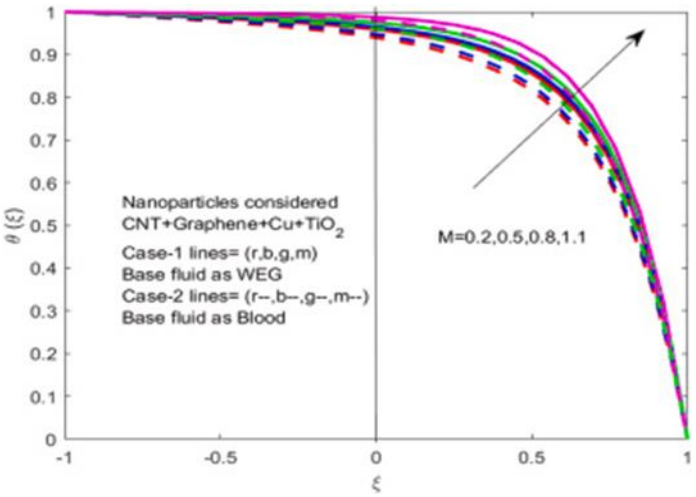

Figure 9. (ξ) with the impact of M

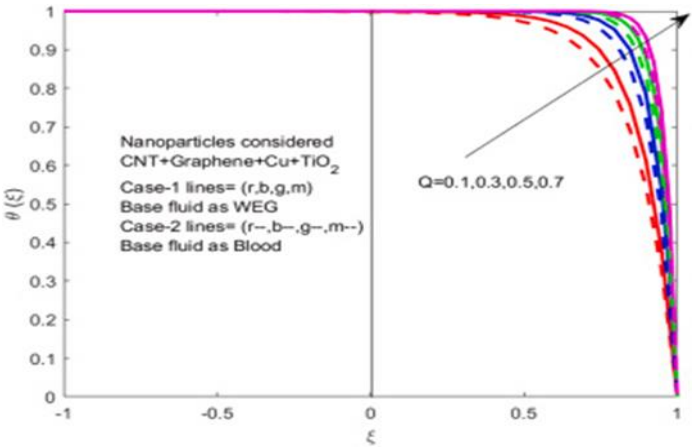

Figure 10. (ξ) with the impact of Q

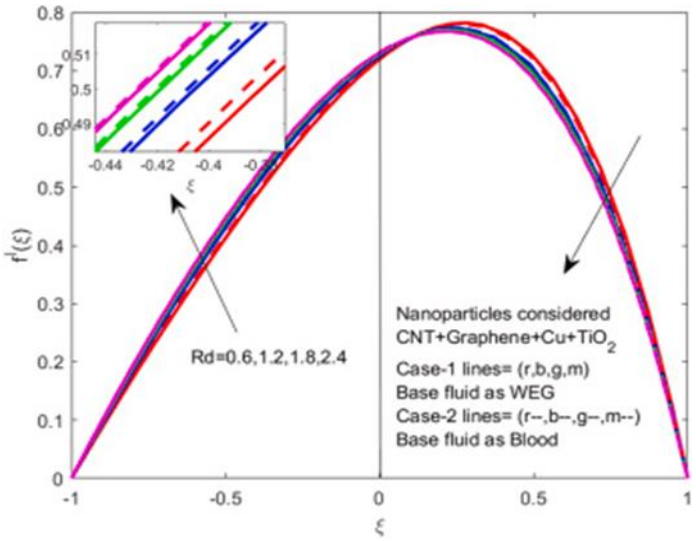

Figure 11. $f'(\xi)$ with the impact of Rd

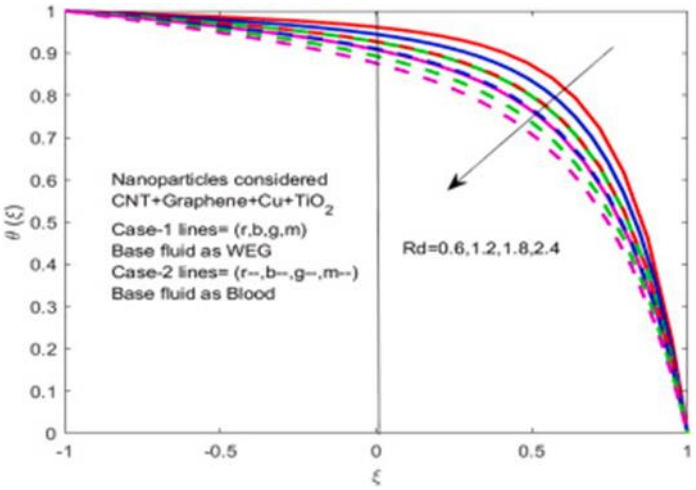

Figure 12. (ξ) with the impact of Rd

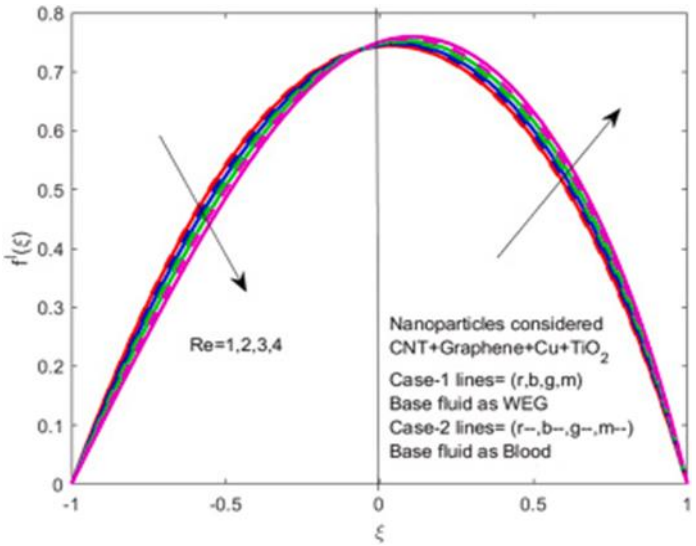

Figure 13. $f'(\xi)$ with the impact of Re

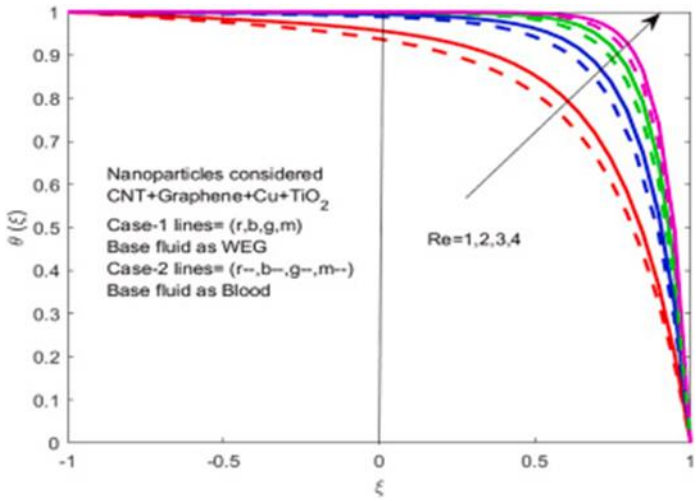

Figure 14. (ξ) with the impact of Re

Adaptive neuro-fuzzy inference system coupled with particle swarm optimization (ANFIS-PSO)

In this study, the ANFIS-PSO technique merges the Adaptive Neuro-Fuzzy Inference System (ANFIS) with Particle Swarm Optimization (PSO) to fine-tune ANFIS parameters, thereby improving the model's prediction accuracy and computational performance. The PSO algorithm efficiently navigates complex search spaces to identify optimal parameter sets.

The Root Mean Square Error (RMSE) of the neural network for Case 1—CNT + Graphene + Cu + TiO_2 nanoparticles in WEG—is reported as 0.0188632 **(Figure 15)**. **Figure 16** shows the ANFIS-PSO training status for this case, while **Figure 17** presents the set of fuzzy inference rules applied.

Figures 18 and 19 illustrate three-dimensional response surfaces of the Nusselt number with Reynolds number (Re = 1–3) and radiation parameter (Rd = 0.6–1.6). The Nusselt number reaches its maximum at Re = 2.0 and Rd = 1.2.

Similarly, **Figures 20 and 21** display 3D surfaces demonstrating how Re (0.6–1.6) and heat source/sink parameter (Q = 0.1–0.3) affect Nusselt number. The peak value is observed at Re = 1.4 and Q = 0.2.

Figures 22 and 23 depict Nusselt number response surfaces under the combined effects of Q (1–3) and Rd (0.1–0.3), with the highest output occurring at Q = 2.0 and Rd = 0.2.

Finally, **Figures 24 and 25** present quiver plots showing the distribution of the Nusselt number across (Re, Rd) and (Rd, Re) planes. These plots provide a clear visualization of the fluid flow patterns and the interactions between key parameters affecting heat transfer performance in CNT + Graphene + Cu + TiO_2/WEG nanofluids.

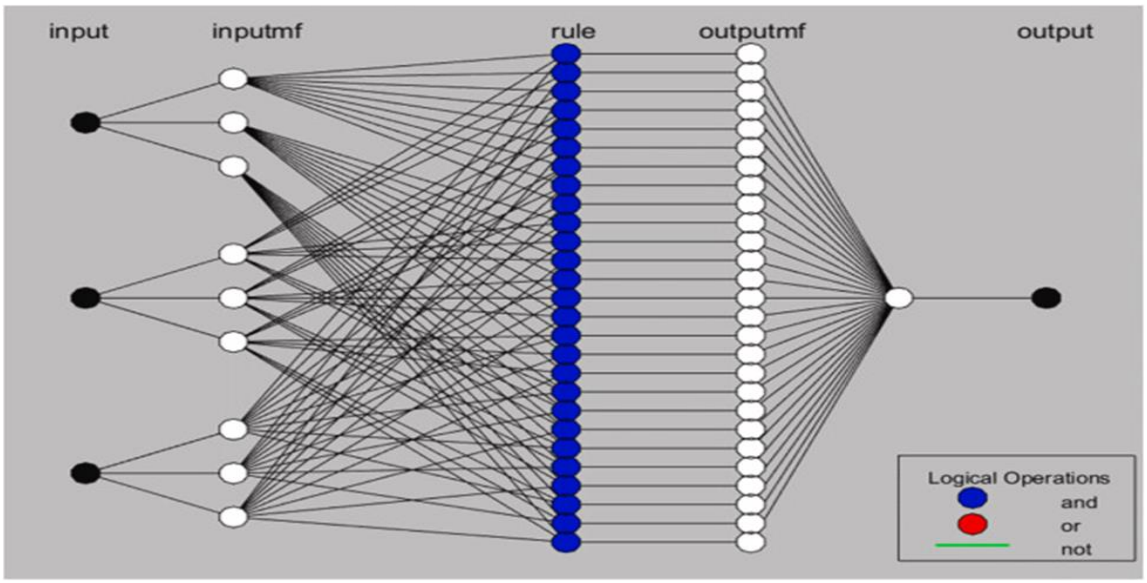

Figure 15. Neural network of ANFIS PSO-case-1, RMSE = 0.0188632.

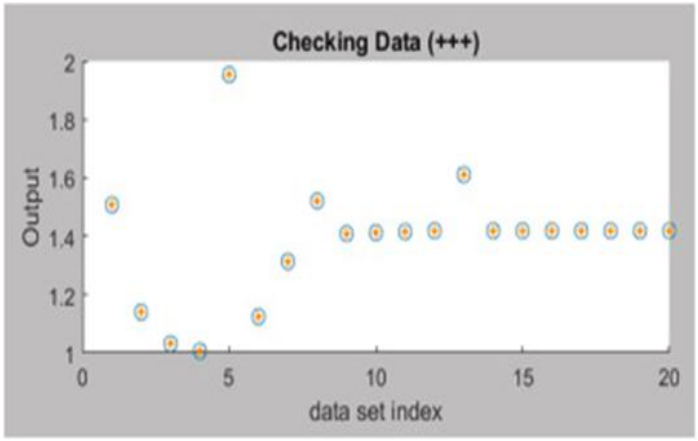

Figure 16. Training state of ANFIS PSO-Case-1.

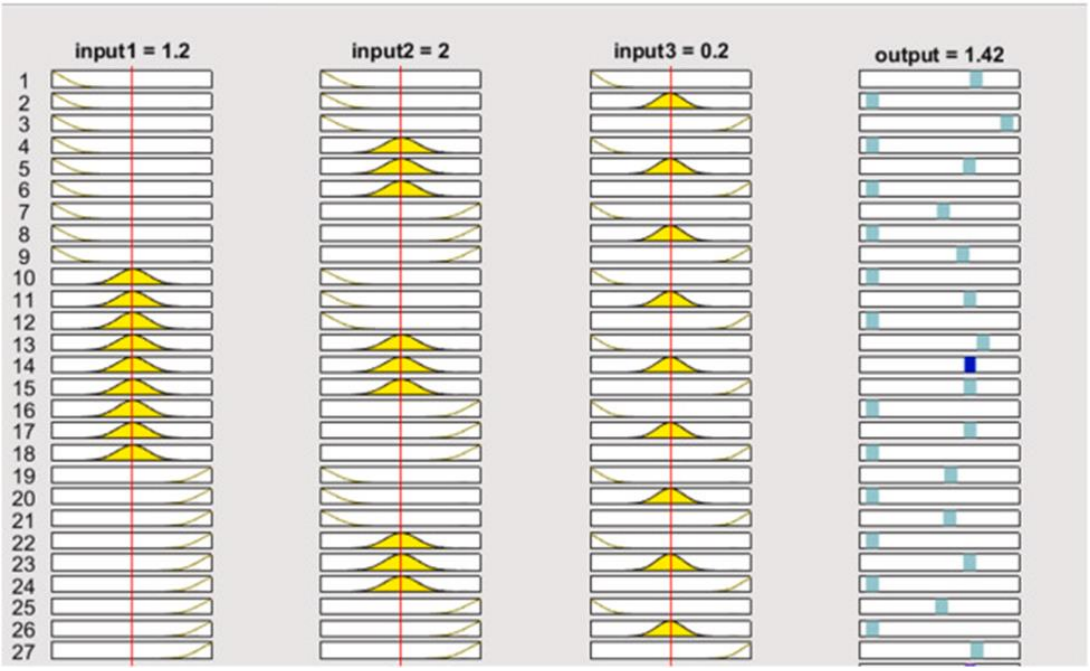

Figure 17. Rule of ANFIS-PSO Case-1.

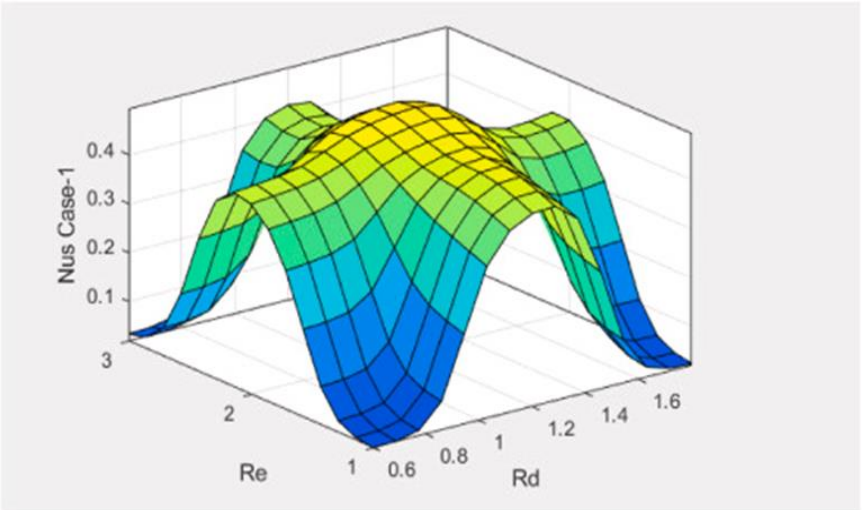

Figure 18. Surface plot of Nu_{s-1} with the impact of Re and Rd

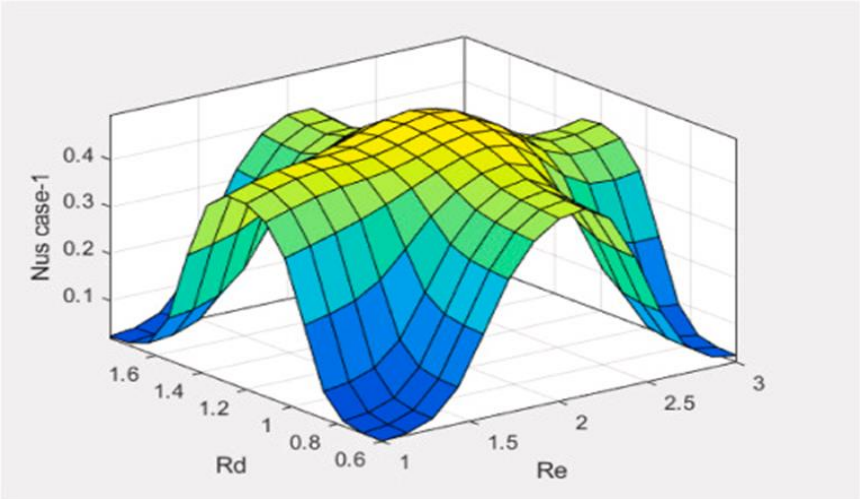

Figure 19. Surface plot of $Nus-1$ with the impact of Rd and Re

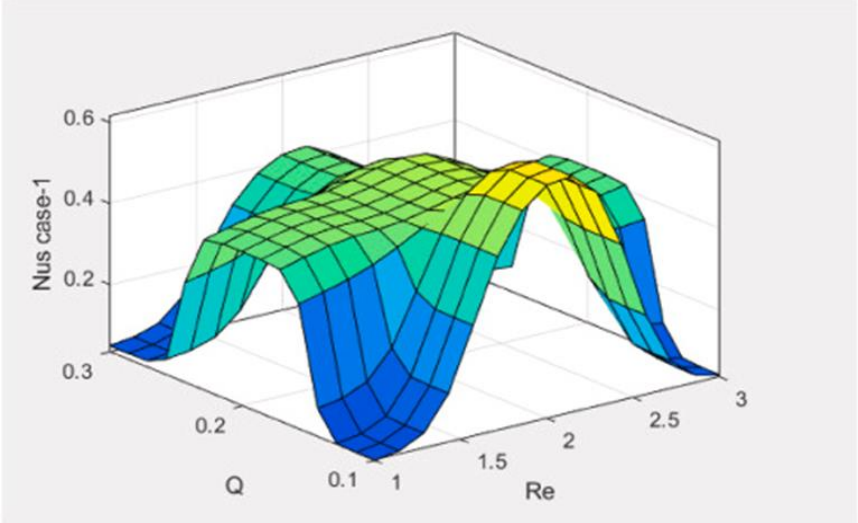

Figure 20. Surface plot of $Nus-1$ with the impact of Q and Re

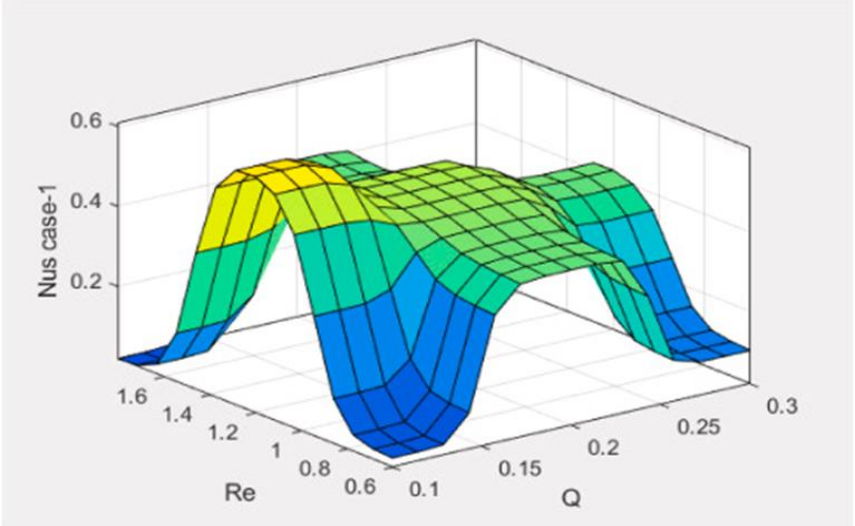

Figure 21. Surface plot of $Nus-1$ with the impact of Re and Q

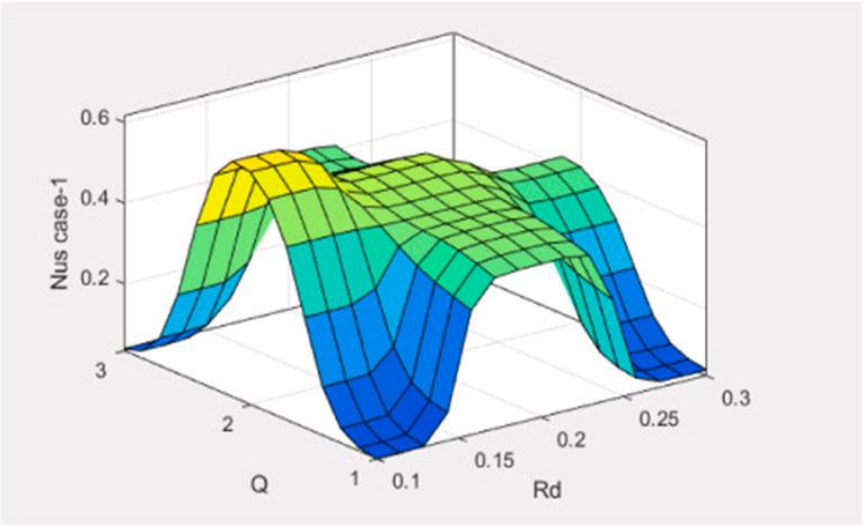

Figure 22. Surface plot of $Nus-1$ with the impact of Q and Rd

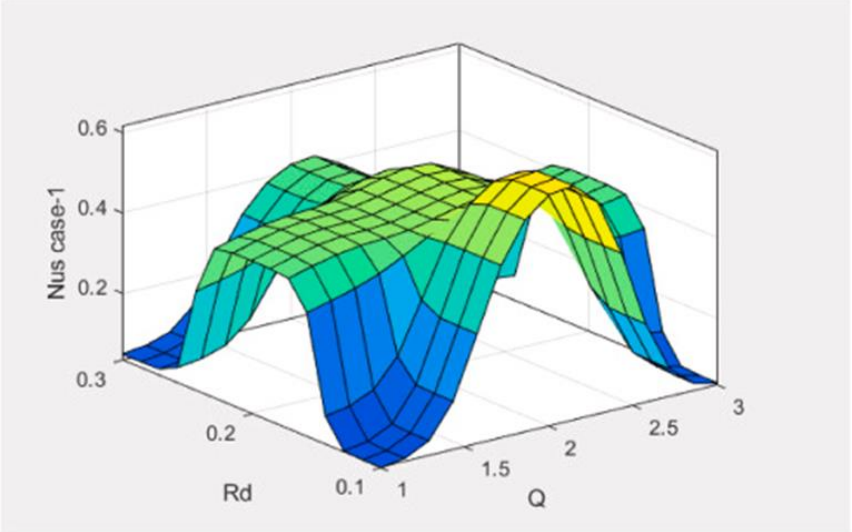

Figure 23. Surface plot of $Nus-1$ with the impact of Rd and Q

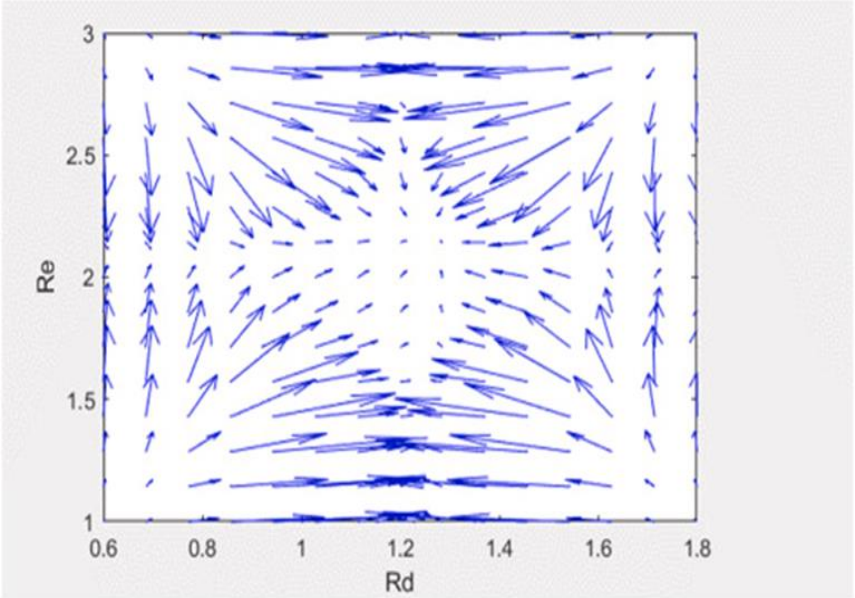

Figure 24. Quiver plot of $Nus-1$ with the impact of Re and Rd

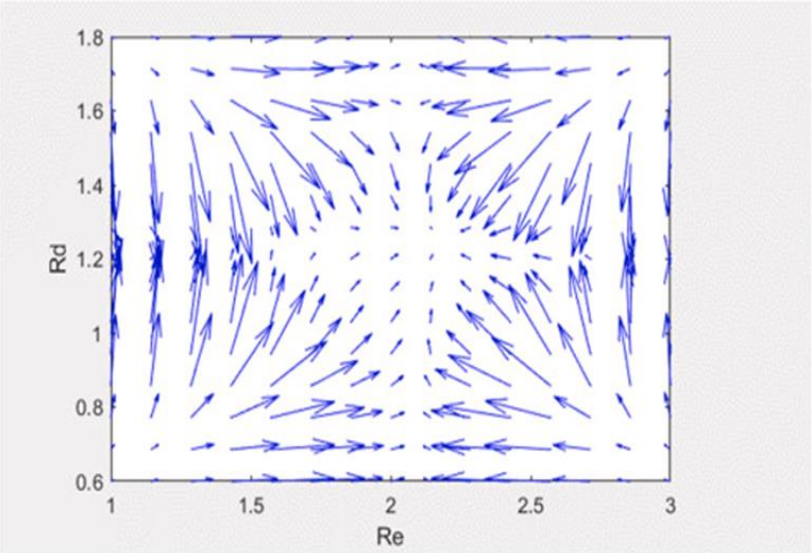

Figure 25. Quiver plot of $Nus-1$ with the impact of Rd and Re

Figure 26 shows that the RMSE of the neural network is 0.0180985 for CNT + Graphene + Cu + TiO_2 nanoparticles in Blood (Case 2). **Figure 27** presents the ANFIS-PSO training progress for Case 2, and **Figure 28** illustrates the fuzzy inference rules applied in this model.

Figures 29 and 30 display three-dimensional response surfaces for the Nusselt number under varying Re (1–3) and Rd (0.6–1.6). The maximum Nusselt number is observed at Re = 2.0 and Rd = 1.2 for the Blood-based nanofluid.

Figures 31 and 32 illustrate the Nusselt number response under Re (0.6–1.6) and Q (0.1–0.3). The highest Nusselt number occurs at Re = 1.4 and Q = 0.2 for Case 2.

Figures 33 and 34 present 3D plots showing the combined effect of Q (1–3) and Rd (0.1–0.3) on Nusselt number. The peak value is obtained at Q = 2.0 and Rd = 0.2 for the Blood-based nanofluid.

Vector fields are visualized using quiver plots, where arrows indicate both magnitude and direction at specific points. These plots are commonly employed to represent fluid flow, electromagnetic fields, and other vector phenomena in engineering and physics.

Figures 35 and 36 show quiver plots for the Nusselt number under (Re, Rd) and (Rd, Re) interactions. These visualizations help predict fluid flow patterns and illustrate the effect of the parameter combinations on heat transfer in CNT + Graphene + Cu + TiO_2/ Blood **(Figure 27)**.

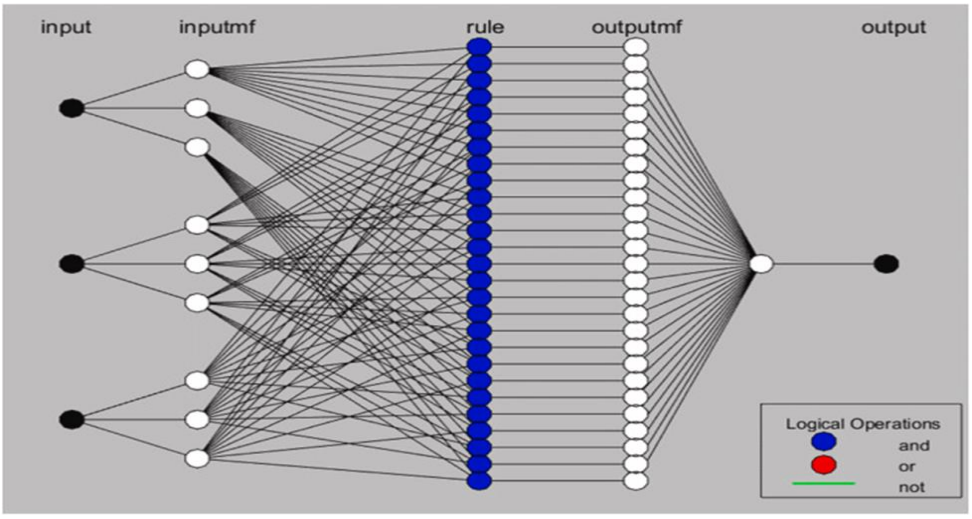

Figure 26. Neural network of ANFIS PSO-case-2, RMSE = 0.0180985.

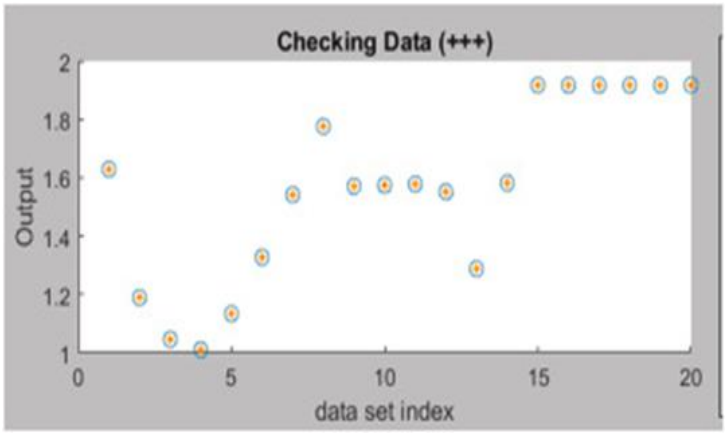

Figure 27. Training state of ANFIS PSO-Case-2.

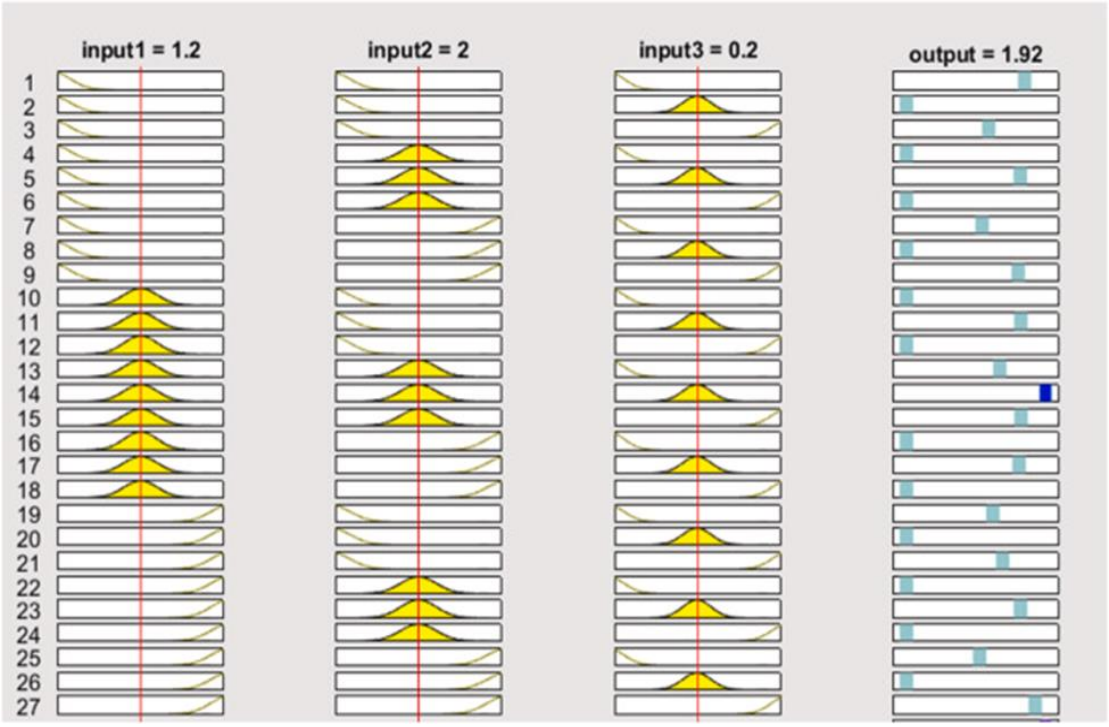

Figure 28. Rule of ANFIS-PSO Case-2.

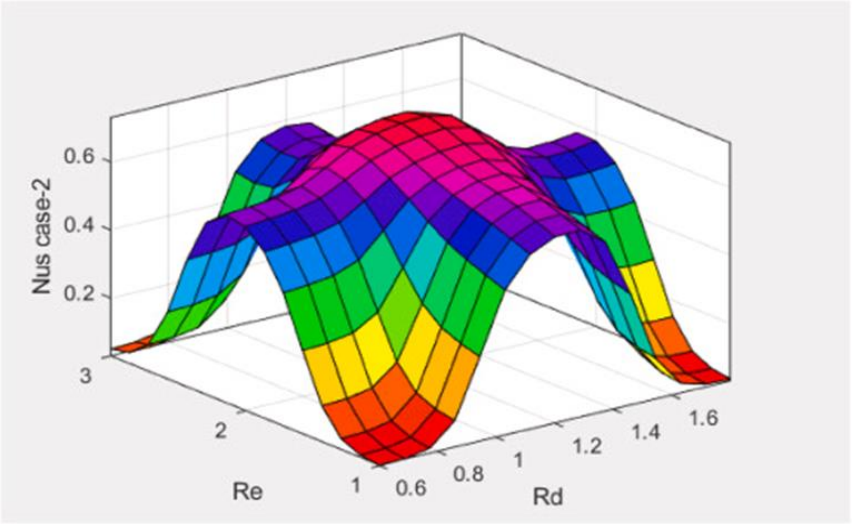

Figure 29. Surface plot of $Nus-2$ with the impact of Re and Rd

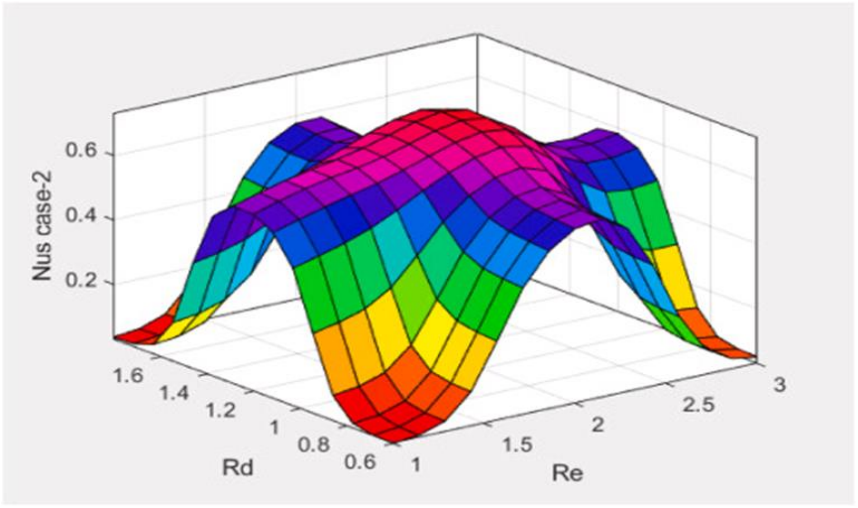

Figure 30. Surface plot of $Nus{-}2$ with the impact of Rd and Re

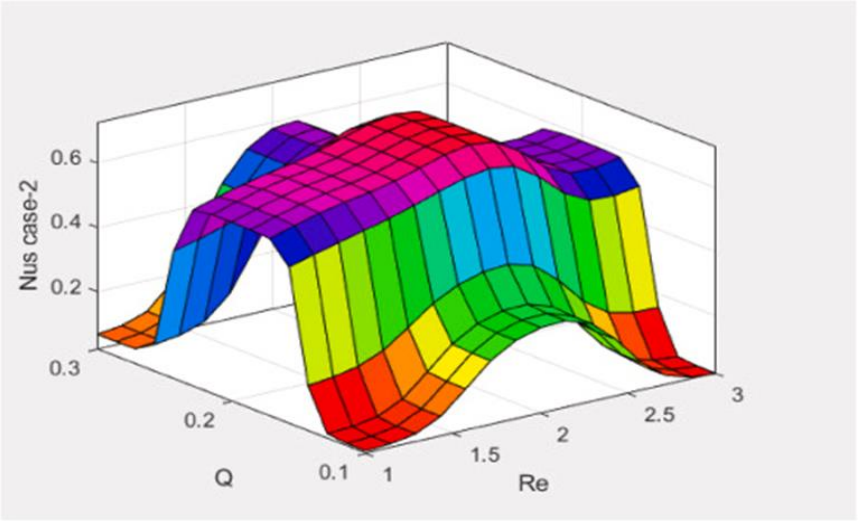

Figure 31. Surface plot of $Nus{-}2$ with the impact of Q and Re

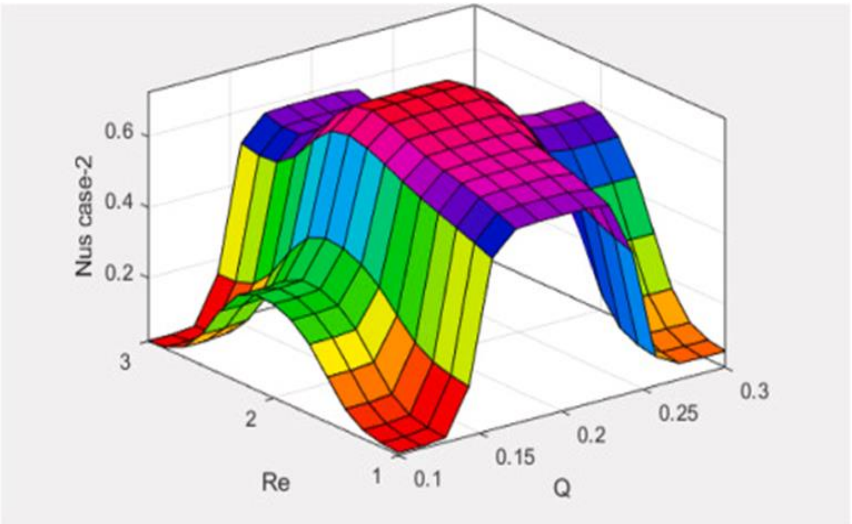

Figure 32. Surface plot of $Nus{-}2$ with the impact of Re and Q

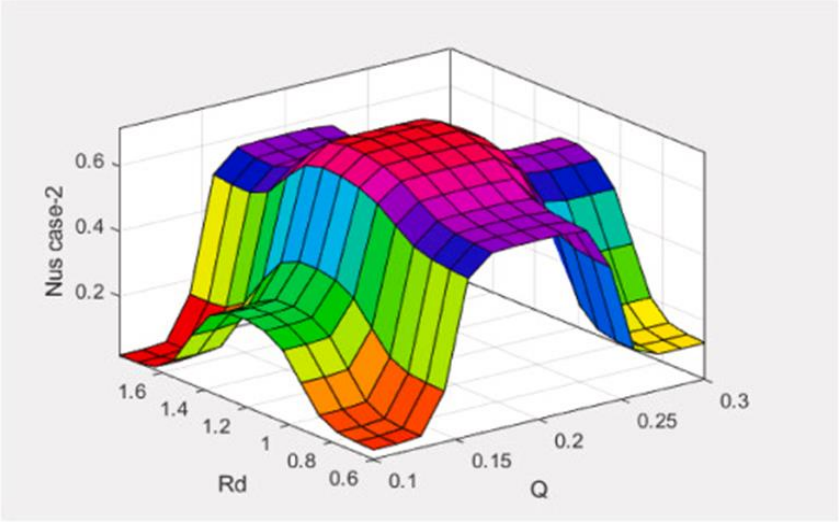

Figure 33. Surface plot of $Nus{-}2$ with the impact of Rd and Q

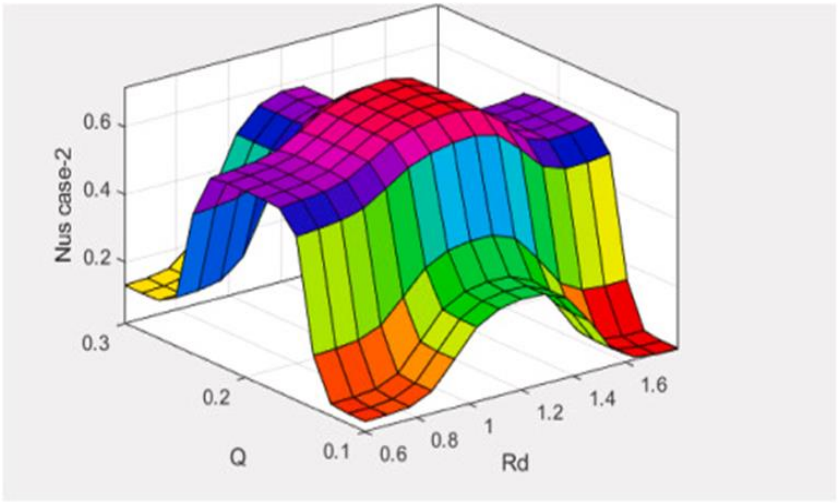

Figure 34. Surface plot of $Nus{-}2$ with the impact of Q and Rd

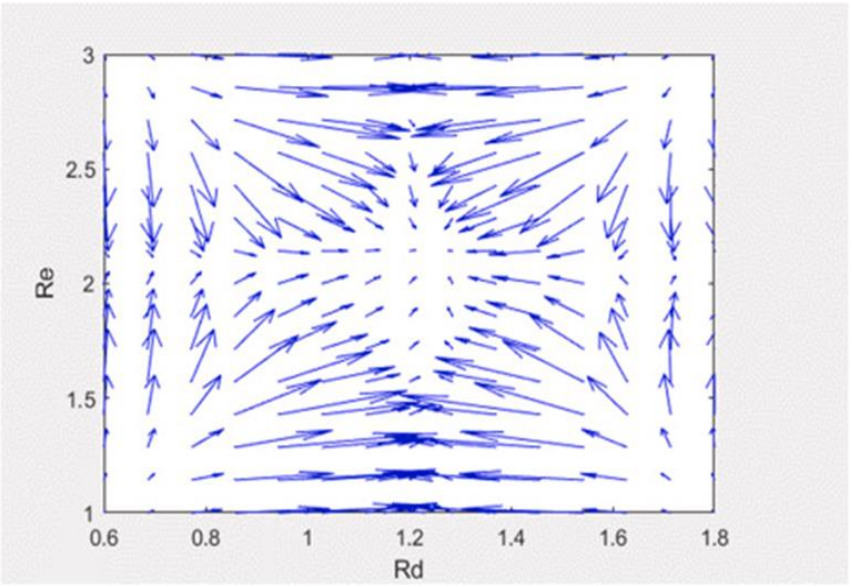

Figure 35. Quiver plot of $Nus{-}2$ with the impact of Re and Rd

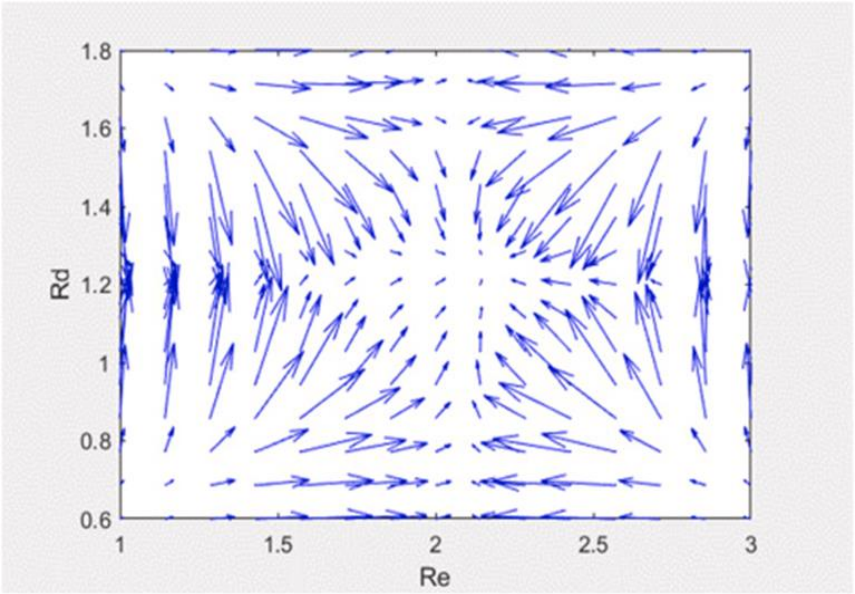

Figure 36. Quiver plot of $Nus-2$ with the impact of Rd and Re

Conclusion

This study established a pivotal link between Cu-CNT-Graphene-TiO_2/WEG-Blood nanoparticles in biomedical applications. Hybrid nanofluid models incorporating bicomponent nanoparticles within a permeable channel remain largely unexplored. This significant research gap highlights an opportunity for further investigation. The present work approached the problem innovatively by considering ANFIS-PSO, Inclined Magnetic, Permeable Reynolds, Porous, Forchheimer, Linear Thermal Radiation, and Buoyancy effects to examine bio-nanofluid behavior. The governing equations were solved numerically using ODE45. A comprehensive evaluation of how inherent physical constraints influence the dynamics of the model was carried out. Additionally, coupling ANFIS with PSO enhanced the predictive performance of the model.

Key findings

- The temperature profile $\theta(\xi)$ increases when Q and M parameters are raised.
- $\theta(\xi)$ decreases as Fr and Rd values increase.
- The concentration profile $\chi(\xi)$ rises with higher M and Re values.
- $\chi(\xi)$ declines when Fr is increased.
- The velocity profile $f'(\xi)$ exhibits mixed behavior as ε, Fr, M, Rd, and Re parameters are varied.
- The RMSE values for ANFIS-PSO, 0.01888632 for Case 1 and 0.0180985 for Case 2, confirm the model's accuracy and reliability.

Practical applications

- **Biomedical Imaging Enhancement:** The optimized model can enhance MRI resolution by analyzing the interaction between hybrid nanofluids and blood under thermal and magnetic effects, leading to more precise diagnostics and improved treatment outcomes.
- **Targeted Drug Delivery Systems**: Insights from this study help regulate nanoparticle movement within the circulatory system, improving the accuracy of targeted drug delivery, which is particularly beneficial in cancer therapy.
- **Thermal Therapy Optimization:** By predicting heat transfer in blood vessels under linear thermal radiation, the model supports more effective thermal therapies, including hyperthermia and cryotherapy, improving both safety and efficacy.
- **Blood Flow Management in Medical Devices:** Understanding blood behavior under magnetic and thermal influences can guide the design of medical devices, enhancing performance in managing blood clots and vascular conditions.

Acknowledgments: None

Conflict of Interest: None

Financial Support: Funding U.F.-G. was supported by the Mobility Lab Foundation, a governmental organization of the Provincial Council of Araba and the local council of Vitoria-Gasteiz. S. Noeiaghdam was supported by the Henan Academy of Sciences (Project No. 241819246).

Ethics Statement: None

References

1. W. He, B. Ruhani, N. Izadpanahi, N.N. Esfahani, A. Karimipour, M. Afrand, Using of artificial neural networks (ANNs) to predict the thermal conductivity of zinc Oxide Silver (50% 50%)/water hybrid Newtonian nanofluid, Int. Commun. Heat Mass Transfer 116 (No) (2020) 104645.
2. D. Toghraie, A comprehensive experimental investigation of thermal conductivity of a ternary hybrid nanofluid containing MWCNTs- titania-zinc oxide/water ethylene glycol (80:20) as well as binary and mono nanofluids, Synth. Met. 268 (2020) 116501.
3. B. Kristiawan, A.I. Rifa'i, K. Enoki, A.T. Wijayanta, T. Miyazaki, Enhancing the thermal performance of TiO2/water nanofluids flowing in a helical microfin tube, Powder Technol. 376 (2020) 254–262.
4. J.C. Kurnia, B. Chaedir, A.T. Wijayanta, A.P. Sasmito, Convective heat transfer enhancement of laminar Herschel Bulkley non-Newtonian fluid in straight and helical heat exchangers with twisted tape inserts, Ind. Eng. Chem. Res. 61 (2022) 814–844.
5. M.M. Bhatti, O.A. B´eg, R. Ellahi, M.H. Doranehgard, F. Rabiei, Electro-magnetohydrodynamics hybrid nanofluid flow with gold and magnesium oxide nanoparticles through vertical parallel plates, J. Magn. Magn Mater. 564 (2022) 170136.
6. S.M. Sait, M.A. Sheremet, H. Oztop, Thermal analysis and entropy generation of magnetic Eyring-Powell nanofluid with viscous dissipation in a wavy asymmetric channel, Int. J. Numer. Methods Heat Fluid Flow (2022) 1609–1636.
7. M.B. Muhammad, F.O. Hakan, E. Rahmat, Study of the magnetized hybrid nanofluid flow through a flat elastic surface with applications in solar energy, Materials 15 (7507) (2022).
8. L. Zhang, N. Tariq, M.B. Mubashir, Study of nonlinear quadratic convection on magnetised viscous fluid flow over a non-Darcian circular elastic surface via spectral approach, J. Taibah Univ. Sci. 17 (2023) 2183702.
9. N. Indumathi, B. Ganga, R. Jayaprakash, A.K.A. Hakeem, Heat transfer of hybrid-nanofluids flow past a permeable flat surface with different volume fractions. J, Appl. Comput. Mech. (2022) 21–35.
10. Z.M. Mburu, S. Mondal, P. Sibanda, An unsteady nanofluid flow past parallel porous plates: a numerical study, Nanosci. Nanotechnology. 12 (2022) 41–55.
11. A. Shaheen, M. Imran, H. Waqas, M. Raza, S. Rashid, Thermal transport analysis of squeezing hybrid nanofluid flow between two parallel plates, Adv. Mech. Eng. 15 (2023) 1–15.
12. R. Mohana Ramana, C. Maheswari, S. Mohiddin Shaw, G. Dharmaiah, U. Fernandez-Gamiz, S. Noeiaghdam, Numerical investigation of 3-D rotating hybrid nanofluid Forchheimer flow with radiation absorption over a stretching sheet, Results in Engineering 22 (2024) 102019, https://doi.org/10.1016/j. rineng.2024.102019.
13. S. Dinarvand, M. Behrouz, S. Ahmadi, P. Ghasemi, S. Noeiaghdam, U. Fernandez-Gamiz, Mixed convection of thermomicropolar AgNPs-GrNPs nanofluid: an application of mass-based hybrid nanofluid model, Case Stud. Therm. Eng. 49 (2023) 103224, https://doi.org/10.1016/j.csite.2023.103224.
14. Bhupendra K. Sharma, P. Sharma, N.K. Mishra, S. Noeiaghdam, U. Fernandez-Gamiz, Bayesian regularization networks for micropolar ternary hybrid nanofluid flow of blood with homogeneous and heterogeneous reactions: entropy generation optimization, Alex. Eng. J. 77 (2023) 127–148, https://doi.org/10.1016/j. aej.2023.06.080.
15. N. Hameed, S. Noeiaghdam, W. Khan, B. Pimpunchat, U. Fernandez-Gamiz, M. Sohail Khan, A. Rehman, Analytical analysis of the magnetic field, heat generation and absorption, viscous dissipation on couple stress

Casson hybrid Nano fluid over a nonlinear stretching surface, Results in Engineering https://doi.org/10.1016/j.rineng.2022.100601.

16. M.S. Khan, S. Mei, Shabnam, U. Fernandez-Gamiz, S. Noeiaghdam, A. Khan, Numerical simulation of a time-dependent electroviscous and hybrid nanofluid with Darcy-forchheimer effect between squeezing plates, Nanomaterials 12 (2022) 876, https://doi.org/10.3390/nano12050876.
17. M.S. Khan, S. Mei, Shabnam, U. Fernandez-Gamiz, S. Noeiaghdam, S.A. Shah, A. Khan, Numerical analysis of unsteady hybrid nanofluid flow comprising CNTs- ferrousoxide/water with variable magnetic field, Nanomaterials 12 (2022) 180, https://doi.org/10.3390/nano12020180.
18. P. Forchheimer, Wasserbewegung durch boden, Z. Ver, Deutsch Ing. 45 (1901) 1782–1788.
19. M. Muskat, R. Wyckoff, The Flow of Homogeneous Fluids through Porous Media, JW Edwards, Michigan, Ann Arbor, 1937.
20. M. Seddeek, Influence of viscous dissipation and thermophoresis on Darcy–Horkheimer mixed convection in a fluid saturated porous media, J. Colloid Interface Sci. 293 (1) (2006) 137–142.
21. M.A. Sadiq, T. Hayat, Darcy–Horkheimer flow of magneto maxwell liquid bounded by convectively heated sheet, Results Phys. 6 (2016) 884–890.
22. T. Hayat, F. Shah, M.I. Khan, A. Alsaedi, Framing the performance of heat absorption/generation and thermal radiation in chemically reactive Darcy- Horkheimer flow, Results Phys. 7 (2017) 3390–3395.
23. G. Rasool, W.A. Khan, S.M. Bilal, I. Khan, MHD squeezed Darcy–Forchheimer nanofluid flow between two h–distance apart horizontal plates, Open Phys. 18 (1) (2020) 1100–1107.
24. Tripathi Bhavya, Kumar Sharma Bhupendra, Two-phase analysis of blood flow through a stenosed artery with the effects of a chemical reaction and radiation, Ric, Mat 73 (2024) 151–177.
25. H. Rajabi Kuyakhi, R.T. Boldaji, M. Azadian, Light hydrocarbons solvents solubility modelling in bitumen using learning approaches, Petrol. Sci. Technol. 39 (4) (2021) 115–131.
26. L. Li, Y. Zhai, Y. Jin, J. Wang, H. Wang, M. Ma, Stability, thermal performance and artificial neural network modelling of viscosity and thermal conductivity of Al2O3- ethylene glycol nanofluids, Powder Technol. 363 (2020) 360–368.
27. R. Tahmasebi Boldaji, H. Rajabi Kuyakhi, N. Tahmasebi Boldaji, M. Rajabzadeh, S. Rashidi, M. Torki, S. Ghazanfari, A comparative study of mathematical and ANFIS models to determine the effect of ultrasonic waves on the viscosity of crude oil, Petrol. Sci. Technol. 40 (2) (2022) 150–165.
28. H. Rajabi Kuyakhi, R. Tahmasebi Boldaji, Developing an adaptive neuro-fuzzy inference system based on particle swarm optimisation model for forecasting Cr(VI) removal by NiO nanoparticles, Environ. Prog. Sustain. Energy 40 (4) (2021) e13597.
29. R.T. Boldaji, H.R. Kuyakhi, Predicting supercritical extraction of st. John's wort by simple quadratic polynomial model and adaptive neuro-fuzzy inference system firefly algorithm, Journal of Analytical Techniques and Research 3 (2) (2021) 14–27.
30. Z.X. Li, F.L. Renault, A.O.C. Go´mez, M.M. Sarafraz, H. Khan, M.R. Safaei, E.P.B. Filho, Nanofluids as secondary fluid in the refrigeration system: experimental data, regression, ANFIS, and NN modelling, Int. J. Heat Mass Transf. 144 (2019) 118635.
31. F. Selimefendigil, H.F. O¨ ztop, Numerical analysis and ANFIS modelling for mixed convection of CNT-water nanofluid-filled branching channel with an annulus and a rotating inner surface at the junction, Int. J. Heat Mass Tran. 127 (2018) 583–599.
32. X. Li, A. Abbasi, K. Al-Khaled, H.F.M. Ameen, S.U. Khan, M.I. Khan, W. Farooq, G. Rasool, K. Guedri, Thermal performance of iron oxide and copper (Fe3O4, Cu) in the hybrid nanofluid flow of Casson material with Hall current via the complex wavy channel, Mater. Sci. Eng., B 289 (2023) 116250.
33. S. Sun, M.I. Khan, K. Al-Khaled, A. Raza, S.S. Abdullaev, S.U. Khan, N. Tamam, S.M. Eldin, Prabhakar fractional approach for enhancement of heat transfer due to hybrid nanomaterial with sinusoidal heat conditions, Case Stud. Therm. Eng. 49 (2023) 103240.
34. B. Mahanthesh, S.A. Shehzad, T. Ambreen, S.U. Khan, Significance of Joule heating and viscous heating on heat transport of MoS 2–Ag hybrid nanofluid past an isothermal wedge, Journal of Thermal Analysis and Calorimetry 143 (2021) 1221–1229.
35. A. Vijayalakshmi, S. Srinivas, Asymmetric nanofluid flow between expanding or contracting permeable walls with thermal radiation, Frontiers in Heat and Mass Transfer 7 (10) (2016) 1–11.

36. H. Shojaie Chahregh, S. Dinarvand, TiO2-Ag/blood hybrid nanofluid flow through an artery with drug delivery applications and blood circulation in the respiratory system, Int. J. Numer. Methods Heat Fluid Flow 30 (11) (2020) 4775–4796.
37. C.S.K. Raju, N.A. Ahammad, K. Sajjan, N.A. Shah, S.J. Yook, M.D. Kumar, Nonlinear movements of axisymmetric ternary hybrid nanofluids in a thermally radiated expanding or contracting permeable Darcy Walls with different shapes and densities: simple linear regression, Int. Commun. Heat Mass Tran. 135 (2022) 106110.